ENDOR and HYSCORE Analysis and DFT-Assisted Identification of the Third Major Stable Radical in Sucrose Single Crystals X-Irradiated at Room Temperature

ARTICLE *in* PHYSICAL CHEMISTRY CHEMICAL PHYSICS · MARCH 2009

Impact Factor: 4.49 · DOI: 10.1039/b816641b · Source: PubMed

7 AUTHORS, INCLUDING:

Ewald Pauwels
Ghent University
56 PUBLICATIONS **666** CITATIONS
SEE PROFILE

Henk Vrielinck
Ghent University
111 PUBLICATIONS **826** CITATIONS
SEE PROFILE

Einar Sagstuen
University of Oslo
176 PUBLICATIONS **2,399** CITATIONS
SEE PROFILE

Sabine Van Doorslaer
University of Antwerp
157 PUBLICATIONS **2,029** CITATIONS
SEE PROFILE

ENDOR and HYSCORE analysis and DFT-assisted identification of the third major stable radical in sucrose single crystals X-irradiated at room temperature†

Hendrik De Cooman,[ab] Ewald Pauwels,[b] Henk Vrielinck,[a] Einar Sagstuen,[c] Sabine Van Doorslaer,[d] Freddy Callens[a] and Michel Waroquier*[b]

Received 23rd September 2008, Accepted 25th November 2008
First published as an Advance Article on the web 13th January 2009
DOI: 10.1039/b816641b

Recently, the chemical structure of two of the three major stable radicals (T2 and T3) produced in sucrose single crystals by X-irradiation at room temperature was identified by comparing Density Functional Theory (DFT) calculations of Electron Magnetic Resonance parameters with experimental results [H. De Cooman, E. Pauwels, H. Vrielinck, E. Sagstuen, F. Callens and M. Waroquier, *J. Phys. Chem. B*, 2008, **112**, 7298–7307]. Ambiguities concerning an unusual proton hyperfine coupling (HFC) tensor prevented the identification of the third major stable radical (T1). In the present work, experimental results of continuous wave Electron Nuclear Double Resonance experiments on sucrose single crystals and Hyperfine Sublevel Correlation Spectroscopy experiments on sucrose powder are presented that lift these remaining ambiguities. Using the final set of experimental HFC tensors and employing advanced DFT calculations, the chemical structure of the T1 radical is established: an allylic-type radical with approximately half of the spin density localised on the C2′ carbon of the fructose unit, involving glycosidic bond cleavage at the fructose side and a concerted formation of a carbonyl group at the C1′ carbon. The electronic structure of the T1 radical is discussed in more detail by means of additional DFT calculations, yielding a better understanding of the peculiar properties of the unusual proton HFC tensor mentioned above.

1. Introduction

Carbohydrates are important constituents of several biological systems including DNA and membrane systems. Elucidating their radiation physics and chemistry is therefore of general importance. Insight into the direct radiation effects occurring in the deoxyribose moiety of DNA is particularly relevant as these may lead to cleavage of sugar–phosphate ester bonds in the DNA backbone (single and double strand breaks) which may in turn result in cell death, cancer and mutagenesis.[1–3] Most of the DNA in a nucleus is rigidly and tightly packed in chromosomes[2] and in this respect, carbohydrate single crystals are appropriate model systems. Consequently, attempts have been made since the early 1970s to identify radiation-induced processes taking place in solid-state carbohydrates. Electron Magnetic Resonance (EMR) experiments have played a major role in this field, as they can provide a wealth of detailed structural and dynamic information. Nonetheless, establishing reliable radical models and reaction pathways is a laborious and not always successful task, not in the least because these compounds do not contain any specific functional group and have considerable conformational freedom. Recently, highly accurate quantum chemical Density Functional Theory (DFT) calculations on extended organic solid-state systems have become feasible due to advances in computing power and density functionals, as well as to the development of new codes for the calculation of EMR parameters. This has given a new and powerful impulse to the study of the radiation chemistry of solid-state carbohydrates.

The disaccharide sucrose (see Fig. 1 (top) for chemical structure) offers an extra advantage as a model system: the ester bond between the two carbohydrate units bears a similarity to the sugar–phosphate ester bond in the DNA backbone. Sucrose is also of particular interest for emergency dosimetry (see *e.g.* ref. 4 and references therein) and has been suggested to be the best, universal material for EPR- (Electron Paramagnetic Resonance) and UV-dosimetry in the region 0.44–160 kGy.[5,6] Ultimately, an advanced understanding of the radiation-induced processes in sucrose may aid in establishing dosimetry protocols.

In single crystals of sucrose three major stable carbon-centred radical species (T1–T3) have been reported to form upon room temperature (RT) X-irradiation.[7] Two of these (T2 and T3) are characterised by very similar HFC tensors, indicating that these species have the same chemical structure but differ only in conformation. Recently, the chemical structure of T2 and T3 has been identified by comparison between the experimental data and the results from advanced Density Functional Theory (DFT) calculations of proton hyperfine coupling (HFC) tensors, although the precise origin of the discrepancy between T2 and T3 was not established.[8] This structure is shown in Fig. 1 (bottom).

For T1, however, a Schonland ambiguity[9] was still present for the HFC tensor $H_{\beta 3}$(T1). Two possible tensors were reported, fitting the available data equally well. These two tensors are

[a] *Department of Solid State Sciences, Ghent University, Krijgslaan 281-S1, B-9000 Gent, Belgium*
[b] *Center for Molecular Modeling, Ghent University, Proeftuinstraat 86, B-9000 Gent, Belgium. E-mail: michel.waroquier@ugent.be; Fax: 003292646697; Tel: 003292646559*
[c] *Department of Physics, University of Oslo, P.O. Box 1048 Blindern, N-0316 Oslo, Norway*
[d] *Department of Physics, University of Antwerp, Universiteitsplein 1, B-2610 Wilrijk-Antwerp, Belgium*
† Electronic supplementary information (ESI) available: Fig. S1–S3. See DOI: 10.1039/b816641b

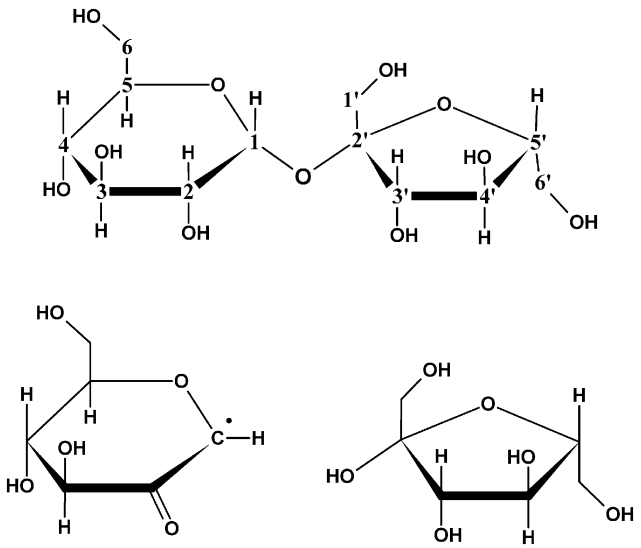

Fig. 1 Top: The chemical structure of the sucrose molecule with the atomic numbering used in the present work. Throughout this work, carbon-bound hydrogen atoms and oxygen atoms are labelled according to the carbon to which they are bound, hydroxy protons according to the oxygen to which they are bound. For example, H3 is the hydrogen at C3, HO3 is the hydroxy proton at C3. Bottom: the chemical structure of the T2/T3 radical species, identified in a previous work.[8]

reproduced in Table 1. Both exhibit unusual features: $^{A}H_{\beta 3}$(T1) has a β-type anisotropy (dipolar components $(-b,-b,+2b)$ with $b > 0$), but a significant negative isotropic component, atypical of β-protons. $^{B}H_{\beta 3}$(T1) has an α-type anisotropy $(-a,0,+a)$, but the values of a and of the isotropic coupling are unusually small for an α-proton and would imply only about 20% spin density on the "α-carbon".[10,11] The overall signs of the principal values are also uncertain since these cannot be determined from the standard cw-EPR and -ENDOR experiments that were performed. Such sign ambiguities are in most cases resolved on the basis of theoretical considerations and/or precedents. As noted above, however, both options are equally unusual in the case at hand.

In the present work, these ambiguities are resolved using both continuous wave Electron Nuclear Double Resonance (cw-ENDOR) and Hyperfine Sublevel Correlation (HYSCORE) spectroscopy. Starting from an initial set of radical models inferred from the final set of T1 proton HFC tensors, DFT calculations based on unconstrained optimisations within a periodic scheme and subsequent cluster single-point calculations of HFC tensors lead to the identification of T1: an allylic-type radical requiring glycosidic bond scission and the concerted formation of a carbonyl group. Finally, the T1 radical structure is studied in more detail with respect to its electronic structure.

Table 1 Two possible HFC tensors ((an)isotropic values in MHz) for the $H_{\beta 3}$ proton HFC of radical T1 in sucrose single crystals X-irradiated at RT, determined from ENDOR measurements at 110 K. The tensors are taken from ref. 7

			Eigenvectors		
	Iso	Aniso	a*	b	c
$^{A}\mathbf{H}_{\beta 3}$	−11.07	−6.50	0.707	−0.245	−0.664
		−3.69	0.383	0.921	0.068
		10.19	0.595	−0.302	0.745
$^{B}\mathbf{H}_{\beta 3}$	11.20	−8.59	0.549	0.231	0.803
		0.59	0.580	−0.797	−0.167
		8.00	0.602	0.558	−0.572

2. Experimental and computational section

2.1 Experimental procedures

Analytical grade (98%) sucrose was obtained from Aldrich and was used to grow single crystals from H_2O or D_2O solutions, as previously described.[7] The crystal structure of sucrose was most accurately determined from a neutron diffraction analysis.[12] The crystals are monoclinic with space group $P2_1$ and a unit cell contains two molecules. The a*bc system (<a*> being orthogonal to both <b> and <c>) was chosen as the orthogonal reference frame, in analogy with previous publications.[7,8] For a certain direction vector, the polar coordinates θ and φ are defined in the current work as the angles measured from the <c>-axis to the vector and the angle measured from the <a*>-axis to the projection of the vector in the <a*b>-plane, respectively. The single crystal was X-irradiated at RT (295 K approximately) to a dose of about 90 kGy using a Philips chromium-anode X-ray tube operated at 60 kV and 40 mA. The sample orientation was determined by stereographic projections and the sample was mounted as described previously.[7] In accordance with previous investigations,[7] the ENDOR spectra were recorded at 110 K approximately 2 days after irradiation, using a Bruker ESP300E spectrometer with an ESP353 ENDOR-TRIPLE extension. The program MAGRES[13,14] was used to derive the HFC tensor from the complete set of previously and currently obtained ENDOR data, as described in *e.g.* ref. 7. The program Easyspin[15] was used for the simulation of the ENDOR angular variations.

X-band pulsed Electron Paramagnetic Resonance (EPR) experiments were performed using a Bruker ESP380E spectrometer (with a microwave frequency of about 9.76 GHz). All experiments were done at RT using a repetition rate of 1 kHz. Instead of the standard HYSCORE scheme,[16] the SMART HYSCORE sequence[17] was used. This not only circumvents the well-known τ-dependent blind-spot effect of standard HYSCORE experiments, but allows, by the appropriate choice of the high-turning-angle (HTA) pulse strength, enhancement of the intensity of specific hyperfine coupling signals. For the SMART-HYSCORE experiments performed on the sucrose powder, X-irradiated at RT, the pulse sequence: HTA–t_1–π–t_2–HTA–τ–π–τ–echo was applied with t_π = 16 ns and HTA pulses with lengths of 40 ns. The proton HFCs of interest are weak (*i.e.* the HFC value is smaller than twice the proton Larmor frequency of $\nu_H \approx 14.8$ MHz), and the matching pulse frequency (ν_1) for this type of coupling is ν_H,[17] but ν_1 = 15.625 MHz was used as this is the value closest to ν_H that can easily be obtained with the present experimental setup. A value of 96 ns was used for τ. The times t_1 and t_2 were changed from 96 ns to 2488 ns in steps of 8 ns. The time-domain HYSCORE spectra were baseline corrected with a third-order polynomial, apodized with a Hamming window and zero filled. The absolute-value spectra were obtained by a two-dimensional Fourier transformation. Because of the large spectral asymmetry *versus* the diagonal, typical for SMART-HYSCORE spectra, the spectra presented in the current work were symmetrised. Time-domain

HYSCORE spectra were simulated using a program developed at ETH Zurich,[18] whereas the frequency-domain simulations were performed using EasySpin.[15]

2.2 Computational procedures

Unless explicitly mentioned otherwise, the computational scheme employed and discussed in ref. 8 was used for the geometry optimisations: periodic calculations were performed with the CPMD software package[19] using an <ab2c> supercell (180 atoms), obtained by doubling the original crystal unit cell in the <c> direction. This supercell is depicted in Fig. 2. A BP86 gradient-corrected density functional[20,21] was used, together with a plane wave basis set (with a maximum kinetic energy of 25 Ry for the plane waves) and ultra-soft pseudopotentials of the Vanderbilt type.[22] No constraints were imposed on the atoms of the supercell during optimisation. For radical fragments I and II (section 3.3), the geometry optimisations were performed in the Gaussian03 program package[23] with a B3LYP functional[24] and a 6–311G(d,p) basis set[25,26] for all atoms.

The single-point calculations of the HFC tensors were always performed within the Gaussian03 program package, also employing the B3LYP functional and a 6–311G(d,p) basis set. In previous publications,[7,8] this type of calculation was performed on a cluster consisting of the radical and ten surrounding sucrose molecules, cut out of the periodically optimised <ab2c> supercell ('full cluster approach'). However, the accuracy of the calculated HFC tensors mainly depends on the accuracy of the radical geometry, as demonstrated in a recent paper by Declerck and co-workers on radicals in fructose single crystals.[27] We made similar observations in a previous work.[8] Therefore, a simpler computational scheme was adopted in the present work for the calculations of HFC tensors in the initial search for a suitable radical model: only the optimised radical molecule (defined in the current work as the molecule on which the unpaired electron is located), cut out of the periodically optimised <ab2c> supercell, was considered ('single molecule approach'). For the radical model yielding the best agreement with the experimental data, however, additional calculations were made using the full cluster approach described above.

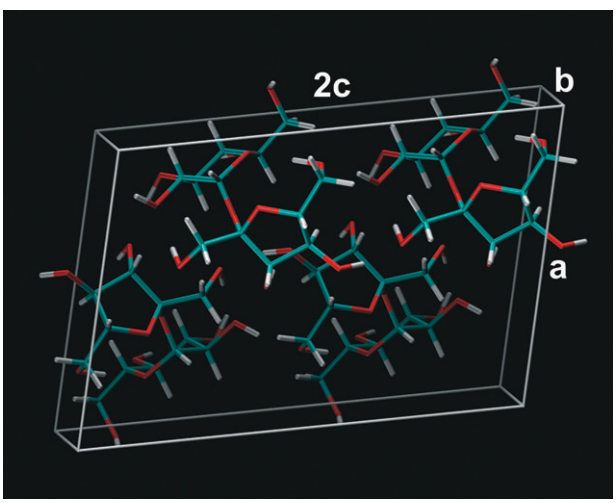

Fig. 2 3D structure of the <ab2c> supercell used for most of the periodic geometry optimisations in the current work, obtained by doubling the crystal unit cell in the <c> direction. The atomic coordinates were taken from ref. 9.

Whenever a comparison is made between calculated eigenvector directions and experimentally determined eigenvector directions or crystal directions, allowed symmetry operations (b → −b and inversion of eigenvectors) are performed to obtain the best possible agreement.

3. Theory

For an $S = 1/2$, $I = 1/2$ system, the nuclear transition frequencies in the two m_S manifolds for a given orientation of the molecule *versus* the external magnetic field are[28]

$$\nu_{\alpha(\beta)} = \sqrt{\left(\frac{A}{2} \pm \nu_I\right)^2 + \left(\frac{B}{2}\right)^2}$$

with ν_I the Larmor frequency, $A = A_{zz}$ and $B = \sqrt{A_{zx}^2 + A_{zy}^2}$ the secular and pseudo-secular hyperfine contributions, respectively. It is clear that, for a given nucleus, the sign of A will determine which of the two nuclear frequencies is the largest. For an $S = 1/2$, $I = 1/2$ system, the HYSCORE spectrum will show cross peaks between the two nuclear frequencies. For the system at hand, namely a system where the unpaired electron is interacting with many protons ($S = 1/2$, $I_n = 1/2$ with n the number of protons), additional HYSCORE cross peaks involving sum frequencies can be observed. Each observable sum frequency $\nu_{\alpha(\beta)}^{\pm}$ corresponds to the sum of basic frequencies within one electron-spin manifold for a particular radical:

$$\nu_{\alpha(\beta)}^{\pm} = \sum_i \nu_{\alpha(\beta)}^i$$

where i runs over the protons with which the unpaired electron interacts. This implies that changing the sign of one of the couplings will alter the corresponding sum frequency and, hence, the position of the HYSCORE cross peak. In most cases, only the cross peaks stemming from sum frequencies between two nuclei are clearly observable in the HYSCORE spectra, the higher multi-nuclei sum peaks having too low intensity. The sum frequencies can thus reveal the relative signs of two HFCs. In the HYSCORE spectra of disordered systems, like the sucrose powder in the case at hand, cross ridges instead of cross peaks are observed, resulting from the simultaneous observation of different molecular orientations. These ridges reflect the anisotropy of the proton HFC tensors and the sum frequency combination ridges again allow for the determination of the relative signs of two proton HFCs belonging to the same radical species.

4. Results and discussion

4.1 Determination of $H_{\beta 3}$(T1)

To determine the correct tensor symmetry of the $H_{\beta 3}$(T1) HFC tensor (tensor A or B in Table 1), ENDOR measurements were carried out in a carefully selected skewed plane (Fig. 3). This method was attempted previously[7] and proved successful for all HFC tensors except $H_{\beta 3}$(T1) because the $H_{\beta 3}$(T1) ENDOR lines could not be resolved at a sufficient number of orientations of the magnetic field in the rotation plane chosen at that time. For the new experiment, a suitable orientation of the rotation plane was first chosen by means of simulations. This orientation

of the skewed plane was then approximately obtained by means of XRD stereographic projections. Afterwards, the plane orientation was more accurately determined using the well known HFC tensors of radical species T1, T2 and T3. As shown in Fig. 3, $^{A}H_{\beta3}$(T1) reproduces the experimental angular variation of the ENDOR signal accurately, whereas $^{B}H_{\beta3}$(T1) clearly does not, allowing for the definitive conclusion that $^{A}H_{\beta3}$(T1) exhibits the correct tensor symmetry. In Table 2, the final $H_{\beta3}$(T1) tensor is presented, for which the data points in the skewed plane were now included in the fitting, resulting in some minor adjustments to the $^{A}H_{\beta3}$(T1) tensor of Table 1.

We are, however, left with the problem of determining the overall sign of $H_{\beta3}$(T1). A common method to determine relative signs of distinct HFCs of a single radical is TRIPLE (also known as double ENDOR) measurements.[29,30] $H_{\beta1}$(T1) is a typical β-proton coupling and its ENDOR signals are well isolated for most orientations, so that it may well serve as 'reference coupling' for the TRIPLE measurements. However,

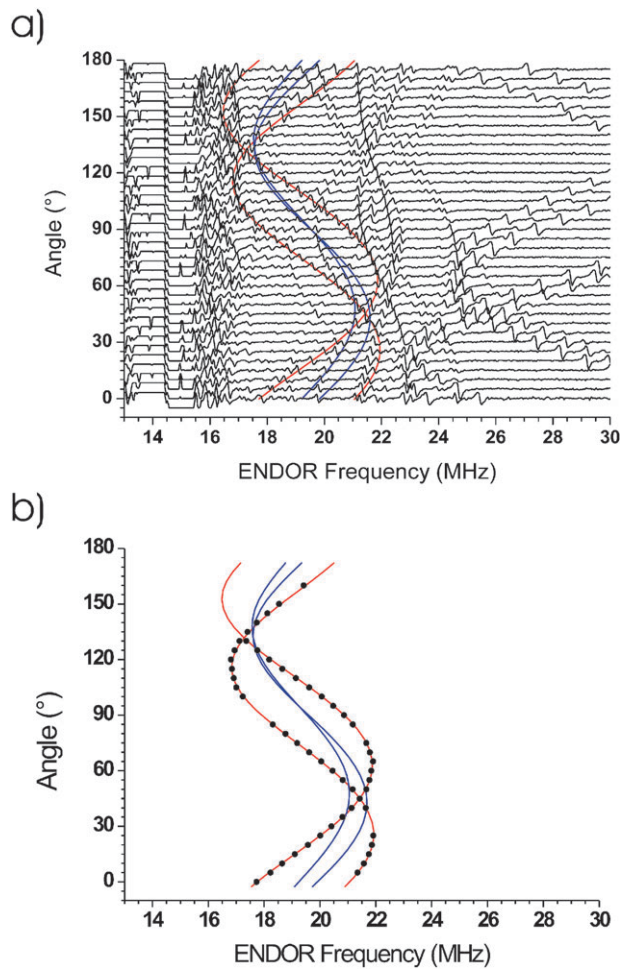

Fig. 3 (a) X-band ENDOR angular variation of sucrose single crystals X-irradiated at RT, recorded approximately 2 days after irradiation. The measurements were performed at 110 K. The spectra are normalised (shifted) to a proton frequency of 14.440 MHz. The direction of the rotation axis is given by θ = 26.1° and φ = 190.3° (definition: see section 2.1). (b) The ENDOR resonance positions of the $H_{\beta3}$(T1) (dots), determined from the angular variation shown in (a). The lines in (a) and (b) are the simulations of the ENDOR angular variations using the $^{A}H_{\beta3}$(T1) (red) and $^{B}H_{\beta3}$(T1) (blue) HFC tensors (Table 1).

Table 2 Final set of proton HFC tensors ((an)isotropic values in MHz) associated with radical T1 in sucrose single crystals X-irradiated at RT, as determined from ENDOR measurements at 110 K. The $H_{\beta1}$(T1) and $H_{\beta2}$(T1) HFC tensors are reproduced from ref. 7. For $H_{\beta3}$(T1), ENDOR resonance positions in an extra, skewed plane (Fig. 3) were included in the fitting, which results in additional small adjustments with respect to HFC tensor $^{A}H_{\beta3}$(T1) reported in ref. 7 (also see Table 1)

				Eigenvectors		
Radical	Proton	Iso	Aniso	a*	b	c
T1	$\mathbf{H}_{\beta1}$	46.80	−3.99	0.616	0.121	−0.778
			−2.38	0.072	0.975	0.209
			6.37	0.784	−0.185	0.592
	$\mathbf{H}_{\beta2}$	15.88	−2.69	0.106	0.825	0.555
			−2.31	0.989	−0.144	0.025
			5.00	0.101	0.546	−0.832
	$\mathbf{H}_{\beta3}$	−11.07	−6.41	0.711	−0.241	−0.660
			−3.73	0.380	0.922	0.073
			10.14	0.591	−0.302	0.748

no significant intensity changes of the $H_{\beta3}$(T1) ENDOR resonances could be observed within the limits of our instrumentation when saturating the $H_{\beta1}$(T1) resonance.

Pulsed EPR experiments proved more successful. SMART HYSCORE spectra, recorded at RT on sucrose powder X-irradiated at RT, are shown in Fig. 4a. As noted in the Experimental Procedure Section, the proton HFCs of interest here (all HFCs of the major stable radicals in sucrose except for $H_{\beta1}$(T1), H_{α}(T2) and H_{α}(T3)) are all weak couplings. In addition to the strong ridge around ν_H corresponding to the correlations between the basic frequencies of the two M_S manifolds, a clear ridge is also present around $2\nu_H$, which corresponds to correlations between sum frequencies. The ridges around ν_H are not dependent on the sign of the HFC, but they could in principle be used to discern $^{A}H_{\beta3}$(T1) from $^{B}H_{\beta3}$(T1). Simulations indeed predict a slightly different shape for the corresponding ridges. In practice, however, this difference is not detectable because of the overlap with the $H_{\beta2}$(T1), $H_{\beta2}$(T2), $H_{\beta3}$(T2), $H_{\beta2}$(T3) and $H_{\beta3}$(T3) HFC resonance lines and with the multitude of distant proton HFC resonance lines near the proton frequency (see Fig. S1 in the ESI).†

The sum frequency ridges, on the other hand, allow for clear discrimination between $^{A}H_{\beta3}$(T1) and $^{B}H_{\beta3}$(T1) as well as determination of the relative signs of $H_{\beta2}$(T1) and $H_{\beta3}$(T1) (which then yields the absolute sign of $H_{\beta3}$(T1) when making the safe assumption that $H_{\beta2}$(T1) has an overall positive sign). In Fig. 4b–e the shape of the combination ridges is simulated for $H_{\beta2}$(T1) with $^{A}H_{\beta3}$(T1) (Fig. 4b and c) and with $^{B}H_{\beta3}$(T1) (Fig. 4d and e) for an overall negative (Fig. 4b and d) or an overall positive (Fig. 4c and e) sign of the $H_{\beta3}$(T1) HFC. Fig. 4 clearly demonstrates that only $^{A}H_{\beta3}$(T1) with the sign as given in Table 1 leads to the appropriate length and shape of the experimentally observed combination ridge. Discerning $^{A}H_{\beta3}$(T1) from $^{B}H_{\beta3}$(T1) is possible here because, in contrast with the ν_H ridge, there is no overlap with ridges originating from other interactions. In Fig. S2 in the ESI,† it is also explicitly shown that the experimentally observed combination ridge does not originate from the T2 or T3 proton HFCs and is not affected by them.

It should be noted that for the simulation above of HYSCORE spectra obtained at RT, HFC tensors determined from ENDOR measurements at 110 K were used. This is certainly reasonable because it was shown in a recent publication

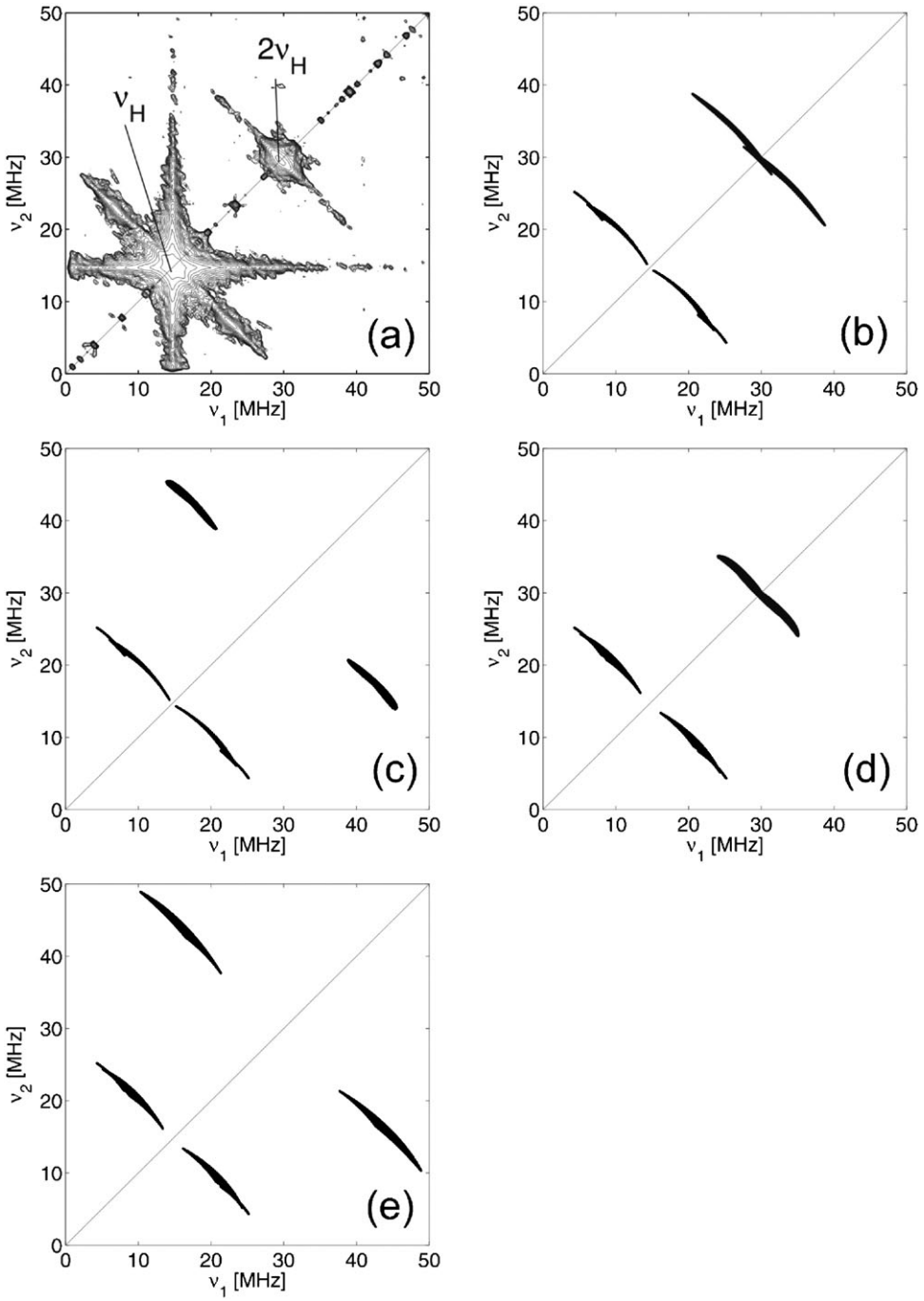

Fig. 4 (a) Experimental X-band SMART HYSCORE spectrum of X-irradiated sucrose powder taken at $B_0 = 346.1$ mT. The measurement was performed at RT. (b–e) Simulation of the correlation ridges expected for a three-spin system $S = 1/2$, $I_{\beta 2} = 1/2$ and $I_{\beta 3} = 1/2$ assuming the HFC tensors of (b) $H_{\beta 2}$(T1) and $^{A}H_{\beta 3}$(T1) (assuming a negative sign of the latter HFC, *cf.* Table 1), (c) $H_{\beta 2}$(T1) and $^{A}H_{\beta 3}$(T1) (assuming a positive sign of the latter HFC) (d) $H_{\beta 2}$(T1) and $^{B}H_{\beta 3}$(T1) (assuming a negative sign of the latter HFC, *cf.* Table 1) (e) $H_{\beta 2}$(T1) and $^{B}H_{\beta 3}$(T1) (assuming a positive sign of the latter HFC). $H_{\beta 2}$(T1) is taken as positive each time.

that the EPR spectrum stays essentially unaltered upon annealing from 110 K to RT.[7] The excellent match between simulated and experimentally obtained sum correlation ridges of Fig. 4 justifies this approach further *a posteriori*.

4.2 Identification of T1

We will now first turn our attention to the other HFC interactions associated with T1 (Table 2). $H_{\beta 1}$(T1) is a typical β-proton HFC. $H_{\beta 2}$(T1) could be due to a β- as well as to a γ-proton HFC interaction because the isotropic component is rather small and the magnitude of the anisotropy is in between those typical of β- and γ-protons. The $H_{\beta 2}$(T1) HFC tensor is in fact quite comparable to the $H_{\beta 1}$ and $H_{\beta 2}$ HFC tensors of radicals T2 and T3.[7] These were shown to arise from γ-protons neighbouring either a ring oxygen or a carbonyl group on which a substantial part of the spin density is localised.[8] It is therefore reasonable to

consider that $H_{\beta 2}$(T1) is also such a proton. As both $H_{\beta 1}$(T1) and $H_{\beta 2}$(T1) exhibit couplings with nearly axial anisotropy, the point dipole approximation should be valid. This implies that the eigenvector associated with the most positive anisotropic coupling is oriented roughly along the line connecting the (main) site of the unpaired spin density with the interacting nucleus. Considering furthermore that experiments on deuterated samples revealed that all T1 HFCs arise from non-exchangeable protons (*i.e.* protons bound to carbons),[7] and assuming that the geometry of the radical does not deviate too much from that of the molecule in the pristine lattice, only three possible radical sites emerge: C1, C4 and C2′ (see Fig. 1 for labelling). In Table 3, an overview is presented of relevant eigenvector directions compared with directions calculated from the pristine crystal structure. The resulting radical model structures are depicted in Fig. 5 as models M1 to M4. For the C1-centred model (M1), only an abstraction of the H1 hydrogen is needed. The C4-centred model (M2) requires hydrogen abstraction of H4 and a concerted formation of a carbonyl group at C3. For the C2′-centred model, there are two possibilities: splitting off a formaldehyde molecule (M3) or cleaving the glycosidic bond at the fructose side (M4).

For each of these four radical structures, periodic geometry optimisations and calculation of EMR parameters in the 'single molecule approach' were performed as described in section 2.2. The calculations did not yield a stable conformation in the case of M3. Additional constraints had to be applied on the formaldehyde molecule in order to prevent spontaneous reattachment and formation of the O1′-centred alkoxy radical. For the calculation of the HFC tensors of M3 the formaldehyde molecule was left out. The HFC tensors calculated for these four models are presented in Table 4. The agreement in HFC tensors is not satisfactory for any of the models. Most notably, (i) none of the models give rise to a HFC interaction that could account for $H_{\beta 3}$(T1) (the HO4 HFC in model M2 has comparable principal values, but $H_{\beta 3}$(T1) is known to arise from a non-exchangeable proton[7]), (ii) the isotropic parts of the γ-proton HFC interactions of models M1 and M3 are very small and even negative, in sharp contrast with the experimentally observed value of approximately 16 MHz for $H_{\beta 2}$(T1), and (iii) for models M2 and M4, the DFT calculations predict HFC interactions (HO4 and H1′a respectively) that are definitely not detected experimentally.

Therefore, variations on the M1–M4 structures need to be considered where these discrepancies could be eliminated. Model M4 gives the best agreement in eigenvector directions for $H_{\beta 1}$(T1) and $H_{\beta 2}$(T1) (Table 4) and it is the only model that can relatively easily be adapted to eliminate its main deficiency, the H1′a HFC. The result is the allylic-type radical model M5 in Fig. 5. Moreover, the carbonyl group present in M5 would enhance the

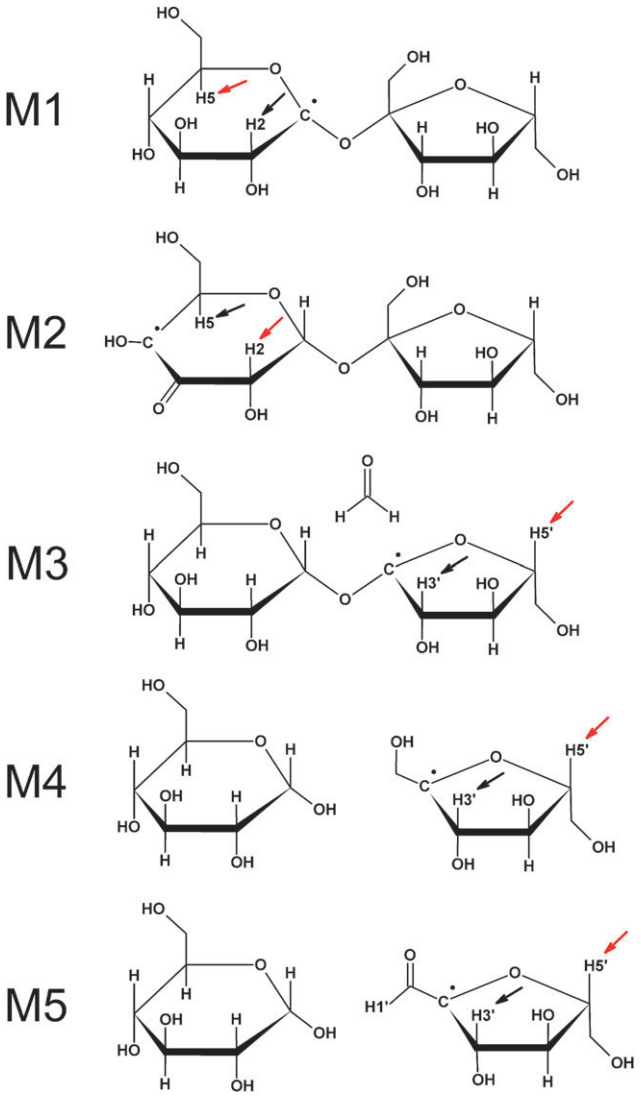

Fig. 5 The chemical structure of radical models M1 to M5, proposed on the basis of agreement between eigenvectors of the $H_{\beta 1}$(T1) and $H_{\beta 2}$(T1) HFC tensors and crystalline directions. The protons relevant for this comparison in directions (see Table 3) are labelled and indicated with arrows (black for $H_{\beta 1}$(T1), red for $H_{\beta 2}$(T1)). DFT calculations indicate that M5 is the actual structure of radical species T1 (Table 5).

g-tensor anisotropy of T1, a feature that has been observed experimentally.[31] The DFT calculations in the single molecule approach on radical species M5 indeed yield HFC tensors that are in excellent agreement on all accounts with the $H_{\beta 1}$(T1) and $H_{\beta 2}$(T1) HFC tensors (Table 5, Approach 1). For $H_{\beta 3}$(T1) some

Table 3 Angle (δ) between crystalline interatomic directions (left hand column) and the eigenvectors associated with the most positive anisotropic coupling values of the HFC tensors specified at the top right hand side (*cf.* Table 2)

			Direction cosines			δ (°)	
	Hydrogen position	Distance (Å)	a*	b	c	$H_{\beta 1}$(T1)	$H_{\beta 2}$(T1)
C1···H2	β	2.14	−0.556	−0.454	−0.696	21.3	
C1···H5	γ	2.74	0.139	−0.647	0.750		15.7
C4···H5	β	2.15	0.542	0.443	0.714	21.6	
C4···H2	γ	2.69	−0.148	0.652	−0.744		16.4
C2′···H3′	β	2.16	0.854	0.420	0.307	21.7	
C2′···H5′	γ	3.01	−0.077	0.731	0.678		13.9

discrepancies remain, in particular with respect to the eigenvectors associated with the smaller anisotropic HFC values. These eigenvector directions are, however, known to be more sensitive to the basis set and level of theory[32] as well as to the precise electronic structure.[33,34] In section 3.3 it will be shown that the latter is substantially modified by the lattice environment. The results presented there are in excellent agreement with the experimental data and leave no doubt that M5 is essentially the correct radical model for T1.

The T1 radical structure (M5, Fig. 5) has key features very similar to the T2/T3 radical (Fig. 1, bottom): a cleaved glycosidic bond and a carbonyl group on which a substantial part of the spin density is localised. This clearly indicates the importance of the glycosidic bond in the radiation chemistry of sucrose. It is a plausible and interesting hypothesis that glycosidic bond cleavage and formation of a carbonyl group are commonly operative mechanisms in X-irradiated polysaccharides, but further work is necessary to test this hypothesis. Also, a very recent study by some of the authors of the current work has revealed that the major stable radical induced by X-ray irradiation at 77 K in single crystals of glucose 1-phosphate has the same chemical structure as the T2/T3 radical. There, a glucose–phosphate bond is broken instead of a glycosidic bond.[35,36] This suggests that those radiation-induced mechanisms may also be operative in glucose-1-phosphate and, by extension, in the sugar–phosphate moiety of DNA. Thus, these results strengthen the validity of sucrose single crystals as a model compound to study the fundamental radiation-induced processes occurring in that moiety. Currently, EMR experiments at low temperatures after *in situ* X-ray irradiation at those temperatures and accompanying DFT calculations are being performed to identify the precursors and unravel the formation mechanisms of the stable sucrose radicals. This will be the subject of a forthcoming publication.

Finally, it might be tempting, based on the chemical structures, to propose that the formation of radical T1 on the one hand and radicals T2 and/or T3 on the other hand are connected, or even that the discrepancies between T2 and T3 can be explained *e.g.* by the presence/absence of a neighbouring T1 radical. However, such radical pairs would yield singlet and triplet states and thus give rise to EPR and ENDOR spectra different from those observed. Moreover, they are not expected to be stable at RT.[37]

Table 4 Proton HFC tensors ((an)isotropic values in MHz) calculated for models M1 to M4 depicted in Fig. 5 as described in section 2.2. δ is the angle between the computed eigenvector directions and the experimentally determined eigenvector directions of the T1 HFC tensors (Table 2)

				Eigenvectors				
Radical model	Proton	Iso	Aniso	a*	b	c	Proton	δ (°)
M1	**H2**	32.85	−6.08	0.808	−0.086	−0.583	$\mathbf{H_{\beta 1}}$	15.9
			−4.78	−0.180	0.906	−0.383		12.4
			10.86	0.561	0.414	0.717		19.8
	H5	−2.60	−4.44	−0.221	0.656	0.721	$\mathbf{H_{\beta 2}}$	23.3
		−1.33	0.936	0.351	−0.032	29.0		
			5.77	0.274	−0.668	0.692		24.2
M2	**H5**	56.60	−3.65	0.576	0.586	−0.570	$\mathbf{H_{\beta 1}}$	43.4
			−2.62	0.750	−0.656	0.083		44.7
			6.27	0.325	0.475	0.818		34.2
	H2	10.86	−2.65	0.885	0.374	0.277	$\mathbf{H_{\beta 2}}$	56.3
			−1.40	−0.412	0.356	0.839		64.0
			4.05	−0.215	0.857	−0.469		33.3
	HO4	−10.12	−8.38	0.868	−0.365	0.336		
			−7.37	0.492	0.553	−0.672		
			15.74	0.060	0.749	0.660		
M3	**H3′**	32.15	−5.82	−0.503	0.863	0.047	$\mathbf{H_{\beta 1}}$	63.2
			−5.23	−0.270	−0.208	0.940		67.7
			11.05	0.821	0.460	0.338		21.7
	H5′	−3.01	−3.31	0.957	−0.184	0.223	$\mathbf{H_{\beta 2}}$	67.8
			−2.29	−0.288	−0.545	0.788		69.9
			5.60	0.024	0.818	0.575		22.8
M4	**H3′**	66.83	−5.22	0.548	0.150	−0.823	$\mathbf{H_{\beta 1}}$	16.3
			−2.70	−0.148	0.986	0.081		17.3
			7.91	0.823	0.077	0.563		6.8
	H5′	6.95	−4.24	−0.211	0.821	−0.531	$\mathbf{H_{\beta 2}}$	6.1
			−2.90	0.940	0.319	0.118		11.7
			7.14	−0.266	0.475	0.839		10.3
	H1′a	56.66	−5.96	0.936	−0.207	0.284		
			−2.77	0.111	0.941	0.319		
			8.73	−0.334	−0.267	0.904		

Table 5 Proton HFC tensors ((an)isotropic values in MHz) calculated for model M5 (Fig. 5) using different computational approaches. The geometry optimisation is performed in an <ab2c> supercell (Approaches 1–3) or in a <2a2b2c> supercell (Approach 4). The calculation of EMR parameters is performed on the (isolated) radical molecule (Approach 1), on the radical molecule and the neighbouring molecule hydrogen-bound to the T1 carbonyl oxygen (Approach 2), or on a cluster consisting of the radical molecule and 10 hydrogen-bound molecules (Approaches 3 and 4). δ is the angle between the computed eigenvector directions and the experimentally determined eigenvector directions of the T1 HFC tensors (Table 2)

				Eigenvectors				
	Proton	Iso	Aniso	a*	b	c	Proton	δ (°)
Approach 1	**H3′**	44.4	−3.79	0.609	−0.056	−0.791	$\mathbf{H_{\beta 1}}$	3.9
			−2.52	−0.092	0.986	−0.140		4.1
			6.31	0.788	0.159	0.595		1.5
	H5′	12.9	−2.60	0.028	0.851	−0.525	$\mathbf{H_{\beta 2}}$	8.0
			−2.20	0.990	0.047	0.130		8.2
			4.80	−0.135	0.524	0.841		2.5
	H1′	−6.5	−5.08	0.617	0.777	−0.123	$\mathbf{H_{\beta 3}}$	70.6
			−3.30	0.575	−0.553	−0.604		70.4
			8.37	0.537	−0.302	0.788		3.9
Approach 2	**H3′**	41.1	−3.69	0.617	−0.094	−0.781	$\mathbf{H_{\beta 1}}$	1.4
			−2.52	−0.076	0.981	−0.178		1.8
			6.22	0.783	0.170	0.598		1.0
	H5′	14.4	−2.49	−0.021	0.847	−0.531	$\mathbf{H_{\beta 2}}$	5.2
			−2.21	0.992	0.083	0.094		5.3
			4.70	−0.124	0.525	0.842		1.9
	H1′	−9.4	−5.69	0.783	0.057	−0.619	$\mathbf{H_{\beta 3}}$	17.8
			−4.58	0.183	0.931	0.316		18.0
			10.27	0.594	−0.361	0.719		3.8
Approach 3	**H3′**	43.5	−3.86	0.624	−0.220	−0.750	$\mathbf{H_{\beta 1}}$	5.9
			−2.27	−0.021	0.954	−0.298		6.0
			6.13	0.781	0.202	0.590		1.0
	H5′	15.4	−2.37	−0.286	0.788	−0.546	$\mathbf{H_{\beta 2}}$	10.6
			−2.24	0.950	0.307	−0.055		10.7
			4.61	−0.124	0.535	0.836		1.5
	H1′	−10.6	−6.81	0.709	−0.136	−0.692	$\mathbf{H_{\beta 3}}$	6.5
			−4.62	0.362	0.912	0.193		7.3
			11.43	0.605	−0.387	0.696		5.7
Approach 4	**H3′**	41.9	−3.74	0.628	−0.198	−0.753	$\mathbf{H_{\beta 1}}$	4.7
			−2.33	−0.032	0.960	−0.280		4.7
			6.07	0.778	0.200	0.596		1.1
	H5′	16.3	−2.40	−0.261	0.797	−0.545	$\mathbf{H_{\beta 2}}$	9.0
			−2.26	0.957	0.286	−0.040		9.2
			4.67	−0.124	0.533	0.837		1.6
	H1′	−11.47	−6.92	0.702	−0.147	−0.697	$\mathbf{H_{\beta 3}}$	5.9
			−4.64	0.356	0.920	0.165		5.8
			11.56	0.617	−0.364	0.698		4.6

4.3 Electronic structure of T1

The electronic structure of the T1 radical, that gives rise to the unusual $H_{\beta 3}$(T1) HFC tensor, will now be discussed in more detail. It is well known that in an allylic radical fragment (Fig. 6a) the central carbon has a substantial negative π-spin density of about −20%, whereas the terminal carbons carry about +60% each.[38,39] The isotropic HFC value of the proton bound to the central carbon is about 12 MHz. The positive sign is expected here because a positive (negative) spin density on a carbon is known to give rise to a negative (positive) isotropic HFC value for an α-proton through standard spin polarisation mechanisms. In the case of the allylic-type radical fragment depicted in Fig. 6b, the spin density on the central (carbonyl) carbon is reduced.[39] For reference purposes, a calculation was carried out on such a radical fragment, yielding a Mulliken spin density of −12% at the carbonyl carbon (Fig. 7a). A negligible isotropic coupling of −0.4 MHz is calculated for the proton bound to the carbonyl carbon, indicating that spin polarisations arising from the various atoms with substantial spin densities cancel each other at that H-atom. However, in the T1 radical a substantial negative isotropic HFC value was found for the $H_{\beta 3}$(T1) HFC (Table 2).

The reason for this qualitative discrepancy was explored by means of additional DFT calculations on radical fragments (Fig. 7a–b) and on the T1 model in various computational approaches

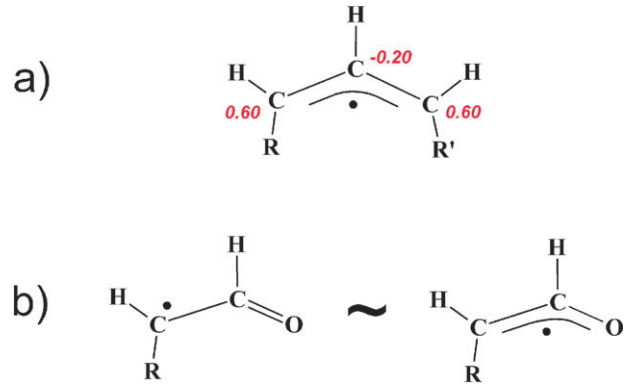

Fig. 6 An allylic (a) and an allylic-type (b) radical fragment. The red italic numbers indicate typical spin densities for the allylic radical fragment.

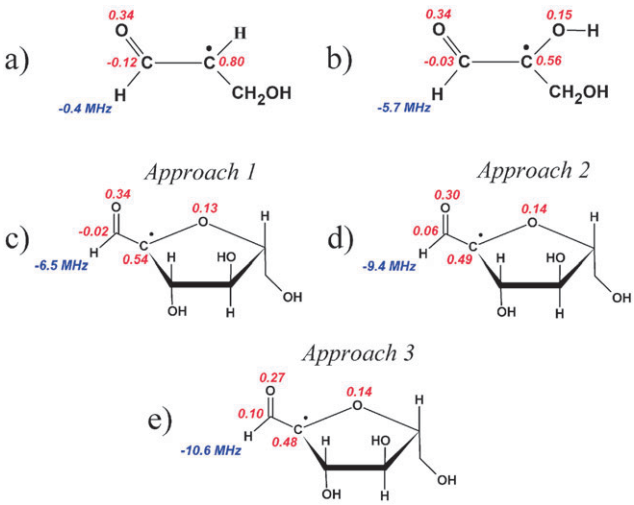

Fig. 7 DFT calculated Mulliken spin densities (red) and isotropic HFC value for the proton bound to the central carbon (blue) for two optimised allylic-type radical fragments (a and b), and for the T1 radical molecule optimised in an <ab2c> supercell (c–e). The single-point calculation was performed not taking the surrounding lattice into account (c), or only taking the molecule into account that is hydrogen-bound to the carbonyl oxygen of the T1 radical (d), or taking the cluster of ten hydrogen-bound molecules into account (e). This corresponds to Approaches 1, 2 and 3 in Table 5 respectively.

(Fig. 7c–e, corresponding to Approaches 1, 2 and 3 in Table 5 respectively). There appear to be essentially two main causes:

1. The presence of the ring oxygen neighbouring C2′ in T1. Comparison of the results of DFT calculations for the radical fragments in Fig. 7a and b shows that the presence of an additional oxygen atom gives rise to a substantial shift in spin densities and an accompanying change in isotropic HFC value for the proton bound to the carbonyl carbon (from −0.4 MHz to −5.7 MHz). The spin densities and the isotropic HFC value of that proton obtained for the radical fragment in Fig. 7b are essentially the same as those obtained from DFT calculations on the isolated T1 radical molecule cut out of the periodically optimised structure (Fig. 7c, Approach 1 in Table 5).

2. The presence of a hydrogen bond between O1′ and the neighbouring lattice. In the lattice, there is a hydrogen bond between the O1′ carbonyl oxygen of the T1 radical, and the HO4′ hydrogen of a neighbouring molecule. In Fig. 7d, the Mulliken spin densities are given for a single-point DFT calculation on the radical molecule and that hydrogen-bound neighbouring molecule, both cut out of the periodically optimised structure (Approach 2 in Table 5). Compared to the calculation on the isolated radical molecule (Fig. 7c and Table 5, Approach 1), there is an increase of positive spin density at C1′ by 8% (from −2% to +6%) and the calculated H1′ HFC tensor is in substantially better agreement with the experimental $H_{\beta 3}$(T1) tensor in all respects. Calculations indicate that subsequently adding hydrogen-bound molecules to the structure on which the single-point DFT calculation is performed systematically improves the agreement with experimental values. Because the effects are minor, only the results for the cluster consisting of the radical molecule and 10 surrounding hydrogen-bound molecules are given (Fig. 7e and Approach 3 in Table 5). In Fig. 8 the spin density distribution as obtained in Approach 3 is visualised.

For reference purposes, calculations were also performed using an even bigger <2a2b2c> supercell for the geometry optimisation and the same cluster as in Approach 3 for the HFC tensor calculation. This is Approach 4 in Table 5. These calculations yield only negligible adjustments to the HFC tensors calculated in Approach 3. Finally, the conformational freedom of the 'dangling' O1-HO1 hydroxy group of the glucose unit was investigated: an energy profile was calculated for the rotation of this hydroxy group about the O1–C1 bond (see Fig. 8 for labelling). This profile indicates that the conformation on which DFT calculations were performed throughout the current work (*cf.* Fig. 8) corresponds to the global minimum. Since it provides no other information relevant for the current discussion, it is reported in the ESI (Fig. S3).†

5. Conclusion

A specifically designed ENDOR experiment at 110 K on a RT X-irradiated sucrose single crystal allowed for the determination

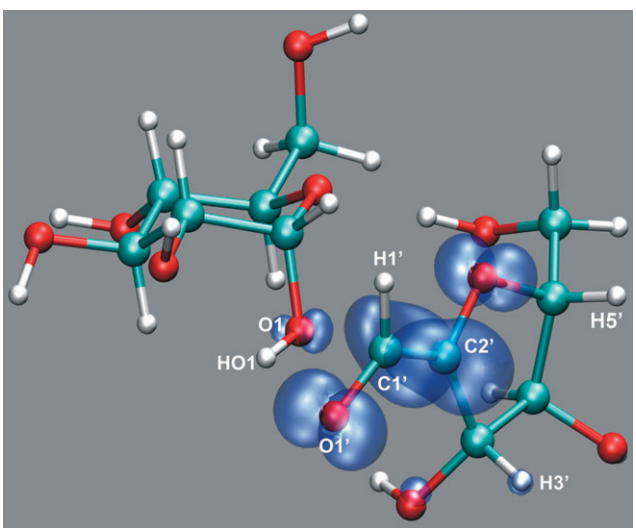

Fig. 8 Optimised structure of radical model M5 (Fig. 5). The spin density distribution, as obtained from the cluster single-point calculation (Approach 3 in Table 5) is visualised by means of a spin density isosurface with ρ = +0.005 (blue).

of the proper Schonland variant of the $H_{\beta 3}$(T1) HFC tensor. HYSCORE experiments at RT on X-irradiated sucrose powder not only confirmed this choice but also readily allowed determination of the sign of this tensor. The obtained HFC tensor has an anisotropy typical of a β-proton, but an uncommon substantial negative isotropic part. Employing advanced DFT calculations, the T1 radical was identified as an allylic-type radical, involving scission of the glycosidic bond and a concerted formation of a carbonyl group. Model DFT calculations provided an explanation for the peculiar $H_{\beta 3}$(T1) HFC tensor in terms of a change in the spin density on the central (carbonyl) carbon of the allylic fragment. The latter is mainly caused by the presence of an adjacent ring oxygen and by hydrogen bonding with a neighbouring molecule in the lattice.

With the identification of the third of three major stable radicals, the EPR spectrum of solid-state sucrose X-irradiated at RT is now largely understood in terms of radical structures. The chemical structures of the three stable radicals are very similar and suggest that glycosidic bond scission and carbonyl group formation may be commonly operative mechanisms in the radiation chemistry of disaccharides, and possibly even in that of the DNA sugar–phosphate moiety.

Acknowledgements

This work was financially supported by the Flemish Research Foundation (FWO-Vlaanderen). The authors acknowledge a Postdoctoral Fellowship (E. Pauwels and H. Vrielinck) and a Research Assistant Fellowship (H. De Cooman) with the same institution.

References

1 W. K. Pogozelski and T. D. Tullius, *Chem. Rev.*, 1998, **98**, 1089–1107.
2 W. A. Bernhard and D. M. Close, in *DNA Damage Dictates the Biological Consequences of Ionizing Irradiation: The Chemical Pathways In Charged Particle and Photon Interactions with Matter: Chemical, Physicochemical, and Biological Consequences with Applications*, ed. A. Mozumder and Y. Hatano, Marcel Dekker, New York, 2003, pp. 431–470.
3 D. Becker, A. Adhikary and M. D. Sevilla, in *The Role of Charge and Spin Migration in DNA Radiation Damage In Charge Migration in DNA Physics, Chemistry and Biology Perspectives*, ed. T. Chakraborty, Springer-Verlag, Berlin Heidelberg, 2007, pp. 139–175.
4 M. Desrosiers and S. Wadley, *Radiat. Prot. Dosim.*, 2006, **118**, 479–481.
5 N. D. Yordanov, V. Gancheva and E. Georgieva, *Radiat. Chem. Phys.*, 2002, **65**, 269–276.
6 N. D. Yordanov and E. Georgieva, *Spectrochim. Acta, Part A*, 2004, **60**, 1307–1314.
7 H. De Cooman, E. Pauwels, H. Vrielinck, A. Dimitrova, N. Yordanov, E. Sagstuen, M. Waroquier and F. Callens, *Spectrochim. Acta, Part A*, 2008, **69**, 1372–1383.
8 H. De Cooman, E. Pauwels, H. Vrielinck, E. Sagstuen, F. Callens and M. Waroquier, *J. Phys. Chem. B*, 2008, **112**, 7298–7307.
9 H. Vrielinck, H. De Cooman, M. A. Tarpan, E. Sagstuen, M. Waroquier and F. Callens, *J. Magn Reson.*, DOI: 10.1016/j.jmr.2008.09.017.
10 W. A. Bernhard, *J. Chem. Phys.*, 1984, **81**, 5928–5935.
11 H. M. McConnell and D. B. Chesnut, *J. Chem. Phys.*, 1958, **28**, 1535.
12 G. M. Brown and H. A. Levy, *Acta Crystallogr., Sect. B: Struct. Crystallogr. Cryst. Chem.*, 1973, **29**, 790–797.
13 W. H. Nelson, *J. Magn. Reson.*, 1980, **38**, 71–78.
14 A. R. Sørnes, E. Sagstuen and A. Lund, *J. Phys. Chem.*, 1995, **99**, 16867–16876.
15 S. Stoll and A. Schweiger, *J. Magn. Reson.*, 2006, **178**, 42.
16 P. Höfer, A. Grupp, H. Nebenführ and M. Mehring, *Chem. Phys. Lett.*, 1986, **132**, 279.
17 L. Liesum and A. Schweiger, *J. Chem. Phys.*, 2001, **114**, 9478.
18 Z. L. Madi, S. Van Doorslaer and A. Schweiger, *J. Magn. Reson.*, 2002, **154**, 181.
19 CPMD V3.11 Copyright IBM Corp 1990–006, Copyright MPI fuer Festkoerperforschung, Stuttgart 1997–001.
20 J. P. Perdew, *Phys. Rev. B*, 1986, **33**, 8822–8824.
21 A. D. Becke, *J. Chem. Phys.*, 1992, **96**, 2155–2160.
22 D. Vanderbilt, *Phys. Rev. B*, 1990, **41**, 7892–7895.
23 M. J. Frisch, G. W. Trucks, H. B. Schlegel, G. E. Scuseria, M. A. Robb, J. R. Cheeseman, J. A. Montgomery, Jr., T. Vreven, K. N. Kudin, J. C. Burant, J. M. Millam, S. S. Iyengar, J. Tomasi, V. Barone, B. Mennucci, M. Cossi, G. Scalmani, N. Rega, G. A. Petersson, H. Nakatsuji, M. Hada, M. Ehara, K. Toyota, R. Fukuda, J. Hasegawa, M. Ishida, T. Nakajima, Y. Honda, O. Kitao, H. Nakai, M. Klene, X. Li, J. E. Knox, H. P. Hratchian, J. B. Cross, V. Bakken, C. Adamo, J. Jaramillo, R. Gomperts, R. E. Stratmann, O. Yazyev, A. J. Austin, R. Cammi, C. Pomelli, J. Ochterski, P. Y. Ayala, K. Morokuma, G. A. Voth, P. Salvador, J. J. Dannenberg, V. G. Zakrzewski, S. Dapprich, A. D. Daniels, M. C. Strain, O. Farkas, D. K. Malick, A. D. Rabuck, K. Raghavachari, J. B. Foresman, J. V. Ortiz, Q. Cui, A. G. Baboul, S. Clifford, J. Cioslowski, B. B. Stefanov, G. Liu, A. Liashenko, P. Piskorz, I. Komaromi, R. L. Martin, D. J. Fox, T. Keith, M. A. Al-Laham, C. Y. Peng, A. Nanayakkara, M. Challacombe, P. M. W. Gill, B. G. Johnson, W. Chen, M. W. Wong, C. Gonzalez and J. A. Pople, *GAUSSIAN 03 (Revision B.03)*, Gaussian, Inc., Wallingford, CT, 2004.
24 A. D. Becke, *J. Chem. Phys.*, 1996, **104**, 1040–1046.
25 R. Krishnan, J. S. Binkley, R. Seeger and J. A. Pople, *J. Chem. Phys.*, 1980, **72**, 650–654.
26 A. D. McLean and G. S. Chandler, *J. Chem. Phys.*, 1980, **72**, 5639–5648.
27 R. Declerck, E. Pauwels, V. Van Speybroeck and M. Waroquier, *J. Phys. Chem. B*, 2008, **112**, 1508–1514.
28 A. Schweiger and G. Jeschke, in *Principles of Pulse Electron Paramagnetic Resonance*, Oxford University Press, Oxford, 2001.
29 R. J. Cook and D. H. Whiffen, *Proc. Phys. Soc.*, 1964, **84**, 845.
30 N. M. Atherton, in *Principles of electron spin resonance*, Ellis Horwood, PTR Prentice Hall, 1993, 429–438.
31 R. Georgieva, L. Pardi, G. Jeschke, D. Gatteschi, L. Sorace and N. D. Yordanov, *Free Radical Res.*, 2006, **40**, 553–563.
32 R. Improta and V. Barone, *Chem. Rev.*, 2004, **104**, 1231–1253.
33 N. Jayatilaka and W. H. Nelson, *J. Phys. Chem. B*, 2007, **111**, 7887.
34 E. Pauwels, V. Van Speybroeck and M. Waroquier, *J. Phys. Chem. A*, 2004, **108**, 11321–11332.
35 H. De Cooman, G. Vanhaelewyn, E. Pauwels, E. Sagstuen, M. Waroquier and F. Callens, *J. Phys. Chem. B*, 2008, **112**, 15045–15053.
36 E. Pauwels, H. De Cooman, E. Sagstuen, F. Callens and M. Waroquier, *J. Phys. Chem. B*, 2008, **112**, 15054–15063.
37 H. C. Box, in *Radiation Effects: ESR and ENDOR analysis*, Academic Press, Inc., New York, 1977.
38 C. Heller and T. Cole, *J. Chem. Phys.*, 1962, **37**, 243–250.
39 L. Salem, in *Molecular orbital theory of conjugated systems*, W.A. Benjamin, New York-Amsterdam, 1966.

